ARTICLE Open Access

0.003°/h bias instability of honeycomb disk resonator gyroscope achieved by mode reversal combined mode deflection control method

Liangqian Chen¹, Qingsong Li¹, Tongqiao Miao¹, Peng Wang¹, Xuhui Zhang¹, Yang Zhang¹, Xuezhong Wu¹ and Dingbang Xiao¹

Abstract

Microelectromechanical systems (MEMS) gyroscopes with higher precision have always been a focal point of research. Due to limitations in resonant structure, fabrication processes, and measurement and control techniques, MEMS gyroscopes with bias instability better than 0.01°/h are still rare and expensive. This paper incorporates electrode machining error and capacitance detection nonlinear error into the gyroscope model, resulting in a more comprehensive bias output model. Based on this, a mode reversal combined mode deflection control method is proposed to eliminate the thermal drift and decrease the bias instability of the gyroscope. Experimental results demonstrate that compared with the traditional force-to-rebalance mode, the new method achieves a 595 times reduction in bias variation during -40 °C to +60 °C temperature cycles and a 6.3 times reduction in bias instability at room temperature. The average bias instability of honeycomb disk resonator gyroscopes can reach 0.003°/h at integration times of 8500 s after applying the new method across three prototypes, which is the best reported performance of the MEMS gyroscope thus far. This paper provides a new paradigm for achieving higher precision MEMS gyroscopes.

Introduction

Nowadays, microelectromechanical systems (MEMS) gyroscopes have broad market prospects in autonomous navigation, north finding, unmanned systems, and precise guidance due to their small size, low power consumption, and mass production capabilities^{1,2}. However, limitations in device-level technology (e.g., materials of resonant structure, fabrication processes, control methods) restrict their potential for high-performance commercial and military applications due to bias drift^{3,4}. Lynch⁵ proved that anisotropic stiffness and anisotropic damping cause the bias drift of symmetrical gyroscopes. After modematching and orthogonal coupling suppression⁶, smaller errors, such as damping variation and capacitance detection nonlinearity, will affect the bias instability (BI) of the gyroscope.

For the bias error caused by damping variation (or quality factor variation), one approach is to reduce the variation of quality factor (Q-factor) with temperature by additional tuning of Q-factor⁷⁻¹¹, thereby reducing the bias thermal drift of the gyroscope. On-chip temperature control can also effectively mitigate O-factor variation due to temperature changes, further decreasing bias thermal drift^{12,13}. Another approach leverages the inherent damping and vibration characteristics of symmetric gyroscopes for self-calibration without additional hardware, such as mode reversal and mode deflection. Mode reversal realizes the difference of the damping asymmetry error by periodically switching the driving mode and the sensing mode. It has been validated as an effective method for self-calibrating bias drift¹⁴⁻¹⁶. Mode deflection corrects the vibration direction to align with the damping axis, eliminating bias drift caused by damping error coupling¹⁷. In addition, polynomial fitting compensation¹⁸ and fuzzy algorithm compensation 19-21 are relatively common bias drift compensation methods. However,

Correspondence: Qingsong Li (liqingsong12@nudt.edu.cn)

¹National University of Defense Technology, Changsha, China

© The Author(s) 2025

Open Access This article is licensed under a Creative Commons Attribution-NonCommercial-NoDerivatives 4.0 International License, which permits any non-commercial use, sharing, distribution and reproduction in any medium or format, as long as you give appropriate credit to the original author(s) and the source, provide a link to the Creative Commons licence, and indicate if you modified the licensed material. You do not have permission under this licence to share adapted material derived from this article or parts of it. The images or other third party material in this article are included in the article's Creative Commons licence, unless indicated otherwise in a credit line to the material. If material is not included in the article's Creative Commons licence and your intended use is not permitted by statutory regulation or exceeds the permitted use, you will need to obtain permission directly from the copyright holder. To view a copy of this licence, visit http://creativecommons.org/licenses/by-nc-nd/4.0/.

these methods heavily rely on the repeatability of the gyroscope, potentially leading to underfitting or over-fitting over time. All the above methods can suppress the bias drift of the gyroscope to some extent. However, in the pursuit of higher precision, the researchers found that some small terms neglected in previous modeling have become the key to limiting the BI of the gyroscope²².

The electrode machining error of the gyroscope is an easily neglected item in dynamic modeling. Electrode angle error²³ or assembly eccentricity error in microhemispherical gyroscope^{24,25} will directly lead to coupling between driving and sensing force signals. This results in scale factor nonlinear errors and additional bias drift²⁶. The detection of nonlinear effects is common in capacitive micro-resonators, and its effect on the scale factor²⁷ (SF) and signal-to-noise ratio^{28,29} (SNR) of the gyroscope has been paid more attention, while its effect on the BI of the gyroscope has rarely been discussed. In fact, the effect of detection nonlinearity on the output of the rate gyro is often ignored as a fixed value under the ideal dynamic model without considering the machining error³⁰. However, due to the electrode error cannot be ignored in actual processing, it is difficult for the gyroscope to maintain perfect output stability over a longer time scale under the combined action of electrode error and detection nonlinear effect.

In this paper, a mode reversal combined mode deflection (MRCMD) control method is presented, which is suitable for a symmetrical vibrating gyroscope. Innovative claims include the following:

- The MRCMD control method is proposed and realized for the first time, which is used to suppress the bias drift caused by the coupling of various minor errors in the gyroscope coupled vibration model.
- 2. The gyroscope vibration model under the coupling condition of electrode manufacturing error and capacitance detection nonlinear error is analyzed. According to the distribution regularity of circumferential harmonics in the model, the method of eliminating the second harmonics by mode reversal and further eliminating the fourth harmonics by mode deflection is proposed to achieve a better suppression of the bias drift of the gyroscope.
- 3. By suppressing multiple harmonics separately, the bias drift of the gyroscope under the combined action of electrode manufacturing error and detection nonlinear error is greatly suppressed. The average BI of 0.003°/h is achieved on three gyroscopes. According to the authors' knowledge, this is the best average BI reported so far MEMS gyroscope.

Compared with other methods mentioned above, this control method can achieve bias suppression of the

gyroscope in the condition of joint nonlinear detection of electrode manufacturing errors, eliminating the need for complex multiple error calibration, and is suitable for any mode-matching MEMS gyroscope.

Results

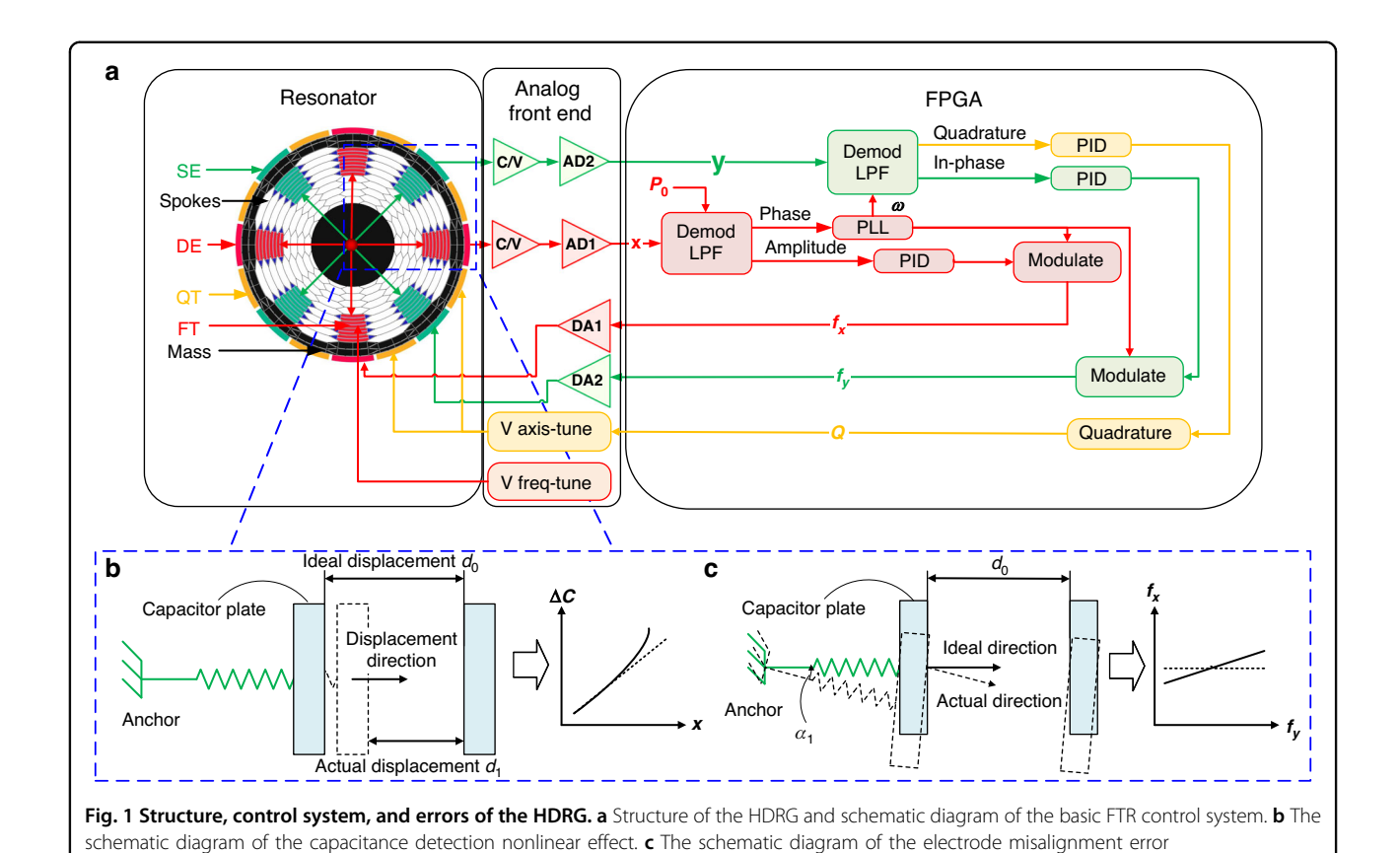
Description of structure and control system

The structure of the honeycomb disk resonator gyroscope (HDRG) and its conventional force-to-rebalance (FTR) mode control system are shown in Fig. 1a. The HDRG mainly consists of multiple honeycomb-shaped ring frames composed of numerous spokes connected with a central anchor point. To achieve a higher Q-factor, a circle of lumped mass is suspended in the outer ring³¹. The inner ring and outer ring of the structure contain a large number of electrodes, including driving electrodes (DE), sensing electrodes (SE), and tuning electrodes for achieving quadrature tuning (QT) and frequency tuning (FT). Details and dimensions regarding the optimization design of HDRG can be found in previous work^{32,33}. HDRG operates in the wine-glass mode with n = 2. The operating frequency of the gyroscope is approximately 4.2 kHz, and the O-factor is about 570 k (ref. 34).

The classical FTR control system consists of four primary control loops: the automatic gain control (AGC) loop, the phase-locked loop (PLL), the quadrature control loop, and the in-phase control loop. These loops respectively control the driving amplitude, phase, quadrature signal, and in-phase signal of the gyroscope. Specifically, the PLL controls the resonator to vibrate at its natural frequency, and the AGC loop keeps the HDRG vibrating with a constant amplitude along the driving axis. The quadrature control loop minimizes the quadrature signal along the sense axis to zero by adjusting the axis-tuning voltage. The in-phase control loop realizes the angular velocity detection by counteracting the vibration displacement caused by the Coriolis force along the sensing axis. In addition, mode matching can be achieved by applying a frequency-tuning voltage to the FT electrodes. Since the geometric dimensions of a single electrode are relatively small compared to the entire resonator, in order to simplify the calculation, parallel-plate capacitors are used for demonstration in the subsequent modeling.

Effects of capacitance detection nonlinear error

The schematic diagram of the capacitance detection nonlinear effect is shown in Fig. 1b. When the gyroscope vibration displacement is small, the detection nonlinearity is weak, and the relationship between the vibration amplitude and the detection voltage can be regarded as linear. However, for a better SNR, a larger vibration displacement is often required. With the increase of vibration displacement, the detection nonlinearity is gradually enhanced, which will cause the detection signal distortion.



For HDRG, all capacitors in the outer ring have the same areas. The driving and sensing of HDRG are both achieved through two pairs of differential capacitors. For the differential capacitance used in HDRG, the Fourier expansion of differential capacitance variation can be

$$\begin{split} \Delta C_d &= 2(C - C') = 2 \left(\frac{\varepsilon A}{d_0 - \Delta x} - \frac{\varepsilon A}{d_0 + \Delta x} \right) \\ &= 4\varepsilon A \frac{\Delta x}{d_0^2} \left[1 + \left(\frac{\Delta x}{d_0} \right)^2 + O\left(\frac{\Delta x}{d_0} \right)^4 \right] \approx 4\varepsilon A \frac{\Delta x}{d_0^2} \left[1 + \left(\frac{\Delta x}{d_0} \right)^2 \right] \\ \Delta C_s &\approx 4\varepsilon A \frac{\Delta y}{d_0^2} \left[1 + \left(\frac{\Delta y}{d_0} \right)^2 \right] \end{split} \tag{1}$$

expressed as:

where, ε is the dielectric constant of the air, A is the equivalent area of the capacitor plate, d_0 is the capacitance gap, Δx and Δy represents the directional vibration displacement of the DE and SE of the resonant structure. After high-frequency carrier demodulation, the detected signal can be expressed as:

$$V_{\rm deo} \approx k_d \left[1 + \left(\frac{\Delta x}{d_0} \right)^2 \right] \Delta x, \ V_{\rm seo} \approx k_s \left[1 + \left(\frac{\Delta y}{d_0} \right)^2 \right] \Delta y$$
 (2)

where, $k_d=-4\varepsilon A\frac{K_1}{d_0^2}, k_s=-4\varepsilon A\frac{K_2}{d_0^2}$ can be regarded as the conversion gain of the two pairs of driving and SE to convert the displacement signal into the voltage signal. K_1 and K_2 represent the circuit gain.

When the gyroscope works in the FTR mode and the angular velocity input is zero. We define $\hat{x} = |x| \cos \omega_d t$, $\hat{y} = 0$ as the displacement of vibration. It is assumed that the gyroscope vibrates in the direction of an arbitrary angle α , then:

$$\begin{bmatrix} \Delta x \\ \Delta y \end{bmatrix} = \begin{bmatrix} x_{\alpha} \\ y_{\alpha} \end{bmatrix} = p \begin{bmatrix} \hat{x} \\ \hat{y} \end{bmatrix} = \begin{bmatrix} \cos \alpha & \sin \alpha \\ -\sin \alpha & \cos \alpha \end{bmatrix} \begin{bmatrix} |x| \cos \omega_d t \\ 0 \end{bmatrix}$$
$$= \begin{bmatrix} |x| \cos \omega_d t \cos \alpha \\ -|x| \cos \omega_d t \sin \alpha \end{bmatrix}$$
(3)

where x_{α} is the vibration displacement in the driving mode direction, y_{α} is the vibration displacement in the sensing mode direction, and p is denoted as the deflection matrix.

Substituting Eqs. (3) into (2), there is:

$$\begin{aligned} V_{deo} &\approx k_d |x| \cos \alpha \cos \omega_d t + k_d \frac{|x|^3}{d_0^2} \cos^3 \alpha \cos^3 \omega_d t \\ &= k_d |x| \cos \alpha \left[1 + \frac{3}{4} \left(\frac{|x|}{d_0} \cos \alpha \right)^2 \right] \cos \omega_d t \\ &+ k_d \frac{|x|^3}{4d_0^2} \cos^3 \alpha \cos 3\omega_d t \\ V_{seo} &\approx -k_s |x| \sin \alpha \left[1 + \frac{3}{4} \left(\frac{|x|}{d_0} \sin \alpha \right)^2 \right] \cos \omega_d t \\ &- k_s \frac{|x|^3}{4d_0^2} \sin^3 \alpha \cos 3\omega_d t \end{aligned} \tag{4}$$

After the signal is demodulated and low-pass filtered, the higher harmonics other than the first harmonic will be removed, so the actual output effective signal is:

$$V_{deo} = N_d |x| \cos \alpha \cos \omega_d t, \ V_{seo} = -N_s |x| \sin \alpha \cos \omega_d t$$
 (5)

where

$$N_d = k_d \left[1 + \frac{3}{4} P_0^2 \cos^2 \alpha \right], N_s = k_s \left[1 + \frac{3}{4} P_0^2 \sin^2 \alpha \right]$$
(6)

represent the nonlinear gain of the driving electrode and the sensing electrode, respectively. In addition, defined $P_0 = |x|/d_0$ as the normalized amplitude of vibration.

Then the displacements of the gyroscope on the driving electrode x and the sensing electrode y can be expressed as:

$$\begin{bmatrix} x \\ y \end{bmatrix} = \begin{bmatrix} N_d & 0 \\ 0 & N_s \end{bmatrix} \begin{bmatrix} \hat{x} \\ \hat{y} \end{bmatrix} = \begin{bmatrix} N_d & 0 \\ 0 & N_s \end{bmatrix} p^{-1} \begin{bmatrix} x_\alpha \\ y_\alpha \end{bmatrix}$$
(7)

For HDRG, the equation of motion can be expressed as³⁵:

$$\begin{bmatrix} \ddot{x} \\ \ddot{y} \end{bmatrix} + \begin{bmatrix} \frac{2}{\tau} + \Delta(\frac{1}{\tau})\cos 2\theta_{\tau} & \Delta(\frac{1}{\tau})\sin 2\theta_{\tau} \\ \Delta(\frac{1}{\tau})\sin 2\theta_{\tau} & \frac{2}{\tau} - \Delta(\frac{1}{\tau})\cos 2\theta_{\tau} \end{bmatrix} \begin{bmatrix} \dot{x} \\ \dot{y} \end{bmatrix}$$

$$+ \begin{bmatrix} \omega^{2} + \omega\Delta\omega\cos 2\theta_{\omega} & \omega\Delta\omega\sin 2\theta_{\omega} \\ \omega\Delta\omega\sin 2\theta_{\omega} & \omega^{2} - \omega\Delta\omega\cos 2\theta_{\omega} \end{bmatrix} \begin{bmatrix} x \\ y \end{bmatrix}$$

$$= \frac{1}{m_{\text{eff}}} \begin{bmatrix} f_{x} \\ f_{y} \end{bmatrix} + 2nA_{g}\Omega \begin{bmatrix} \dot{y} \\ -\dot{x} \end{bmatrix}$$

$$(8)$$

where

$$\omega^{2} = \frac{\omega_{1}^{2} + \omega_{2}^{2}}{2}, \ \omega \Delta \omega = \frac{\omega_{1}^{2} - \omega_{2}^{2}}{2}, \ \frac{2}{\tau} = \frac{1}{\tau_{1}} + \frac{1}{\tau_{2}},$$

$$\Delta \left(\frac{1}{\tau}\right) = \frac{1}{\tau_{1}} - \frac{1}{\tau_{2}}$$
(9)

 m_{eff} is the effective mass of the HDRG, A_g is the angular gain, Ω is the angular velocity, ω is the average natural frequency, ω_1 and ω_2 are the natural frequency along the two stiffness axes, τ is the average damping time constant, τ_1 and τ_2 are the damping time constants along the two damping axes, θ_{ω} is the deflection angle (DA) of the stiffness axis, θ_{τ} is the DA of the damping axis, and n is the modal number, f_{τ} and f_{τ} represent the driving and sensing force.

Under the condition of zero angular velocity input, substituting Eqs. (7) into (8), when the gyroscope works in the FTR mode, the closed-loop axis-tuning voltage will suppress the quadrature signal to zero, and the solution can be obtained:

$$\begin{split} \Omega_{ZRO}(\alpha) &= \frac{1}{2nA_g} \left[\Delta \left(\frac{1}{\tau} \right) \sin 2(\theta_\tau - \alpha) \left(1 + \frac{3}{8} P_0^2 \right) \right. \\ &\left. - \frac{1}{\tau} \frac{3}{16} P_0^2 \sin 4\alpha + \left[\frac{3}{8} P_0^2 \cos 2\alpha \right] \Delta \left(\frac{1}{\tau} \right) \sin 2\theta_\tau \right] \end{split} \tag{10}$$

The circumferential zero-rate output (ZRO) of the HDRG can be expressed as the superposition of the second and fourth harmonics related to the mode angle α . As shown in Fig. 2a, the circumferential distribution of bias under different P_0 conditions can be seen through the simulation of numerical analysis. With the increase of P_0 , the fourth harmonics are gradually excited and affect the circumferential distribution of bias. Similarly, the circumferential distribution of bias at different θ_{τ} angles is shown in Fig. 2b. θ_{τ} mainly affects the circumferential distribution of second harmonics.

Effects of electrode machining error

The schematic diagram of electrode misalignment error is shown in Fig. 1c. Due to the limitation of micromachining technology level, electrode errors in microgyroscope machining are still unavoidable. In the FTR mode, the force coupling error caused by electrode misalignment error can be expressed as:

$$\begin{bmatrix} \hat{f}_x \\ \hat{f}_y \end{bmatrix} = \begin{bmatrix} \cos \alpha_1 & -\sin \alpha_2 \\ \sin \alpha_1 & \cos \alpha_2 \end{bmatrix} \begin{bmatrix} f_x \\ f_y \end{bmatrix}$$
 (11)

where α_1 is the angle error of the DE, and α_2 is the angle error of the SE.

Similarly, assuming that the gyroscope vibrates in the direction of any circumferential angle α , then:

(9)
$$\begin{bmatrix} f_{x\alpha} \\ f_{y\alpha} \end{bmatrix} = \begin{bmatrix} \cos(\alpha - \alpha_1) & \sin(\alpha - \alpha_2) \\ -\sin(\alpha - \alpha_1) & \cos(\alpha - \alpha_2) \end{bmatrix} \begin{bmatrix} f_x \\ f_y \end{bmatrix} = r \begin{bmatrix} f_x \\ f_y \end{bmatrix}$$
 (12)

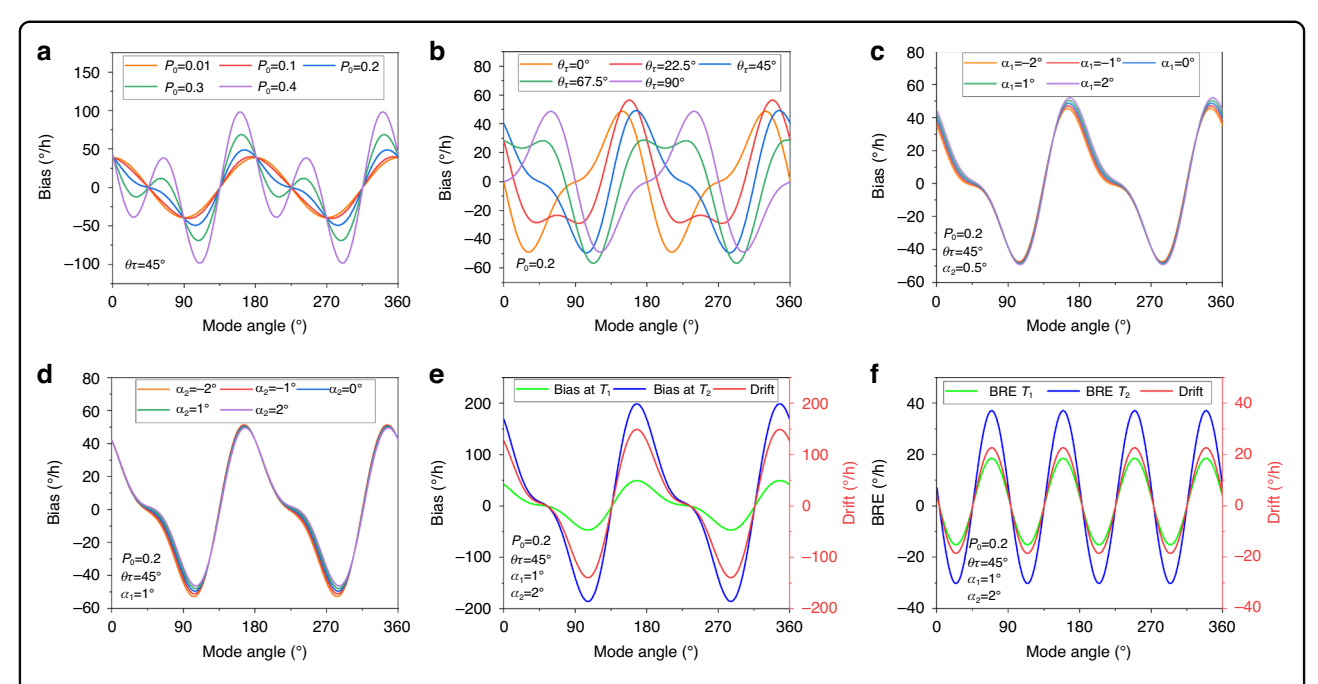


Fig. 2 Simulation results of HDRG structural parameters. a Simulation results of P_0 under different mode angles. **b** Simulation results of θ_{τ} under different mode angles. **c** Simulation results of a_1 under different mode angles. **d** Simulation results of a_2 under different mode angles. **e** Simulation results of bias in FTR mode at different temperatures and drift under different mode angles. **f** Simulation results of BRE after mode reversal at different temperatures and drift under different mode angles.

Denote r^{-1} as the new coupled deflection matrix replacing the deflection matrix p in Eq. (7), then:

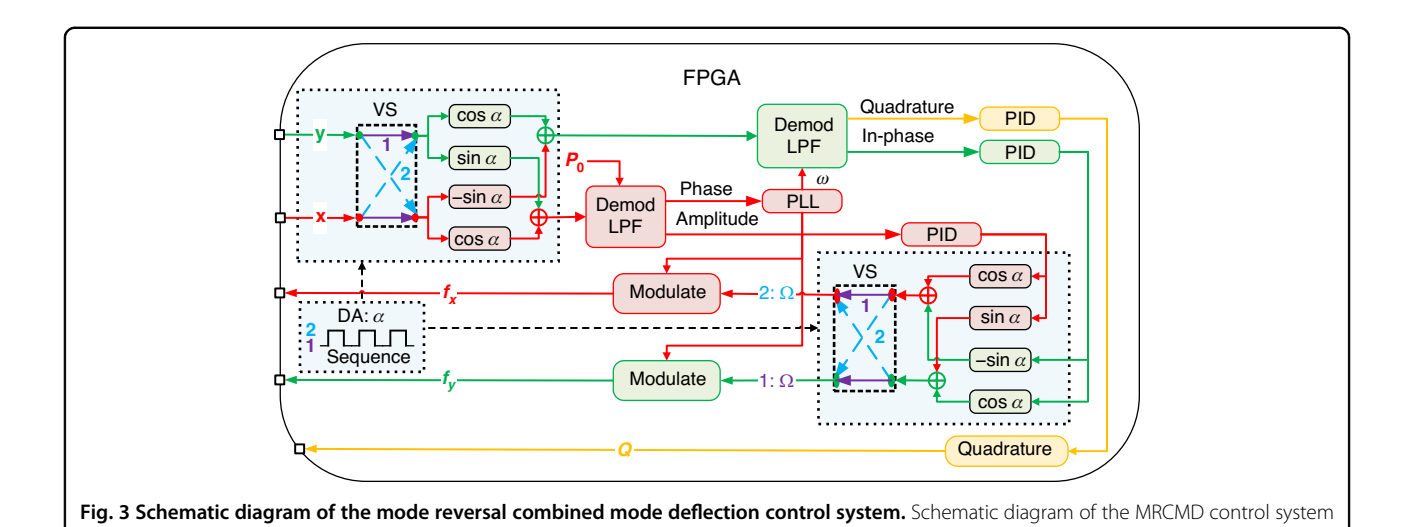
$$\begin{bmatrix} x \\ y \end{bmatrix} = \begin{bmatrix} N_d & 0 \\ 0 & N_s \end{bmatrix} \begin{bmatrix} \hat{x} \\ \hat{y} \end{bmatrix} = \begin{bmatrix} N_d & 0 \\ 0 & N_s \end{bmatrix} r \begin{bmatrix} x_\alpha \\ y_\alpha \end{bmatrix}$$
(13)

In this way, the dynamic equation model is obtained when both the detection nonlinear error and the electrode angle error are considered. Under the condition of zero angular velocity input, substituting Eqs. (13) into (8), when the gyroscope works in the FTR mode, the closed-loop axis-tuning voltage will suppress the quadrature signal to zero, and the solution can be obtained:

The influence of α_1 and α_2 on the circumferential distribution of bias is shown in Fig. 2c, d. With the further introduction of angular errors, the circumferential distribution of bias becomes too complex to predict. It is easy to find that when the two errors are coupled together, it is difficult to analyze and identify one of the errors separately. Naturally, such a complex equation can also be viewed as a superposition of a constant and the second and fourth harmonics associated with the mode angle α :

$$\begin{split} \Omega_{ZRO}(\alpha) &= \frac{1}{2nA_g} \frac{1}{4 \, \cos(\alpha_1 - \alpha_2)} \\ &\cdot [A \, \sin(4\alpha + \varphi_1) + B \, \sin(2\alpha + \varphi_2) + C] \end{split} \tag{15}$$

$$\Omega_{ZRO}(\alpha) = \frac{1}{2nA_g} \frac{1}{4\cos(\alpha_1 - \alpha_2)}
- \Delta(\frac{1}{\tau})[\sin(2\alpha + 2\theta_\tau - \alpha_1 - \alpha_2) + \sin(2\alpha - 2\theta_\tau - \alpha_1 - \alpha_2)](2 + \frac{3}{4}P_0^2)
+ \Delta(\frac{1}{\tau})[\sin(2\theta_\tau + \alpha_1 - \alpha_2) - \sin(2\theta_\tau - \alpha_1 + \alpha_2)](2 + \frac{3}{4}P_0^2)
+ \Delta(\frac{1}{\tau})[-\sin 2(\alpha - \theta_\tau - \alpha_1) + \sin 2(\alpha + \theta_\tau - \alpha_1)](1 + \frac{3}{4}P_0^2\sin^2\alpha)
+ \Delta(\frac{1}{\tau})[-\sin 2(\alpha - \theta_\tau - \alpha_2) + \sin 2(\alpha + \theta_\tau - \alpha_2)](1 + \frac{3}{4}P_0^2\cos^2\alpha)
+ \frac{4}{\tau}[-\sin(2\alpha - \alpha_1 - \alpha_2) + \sin 2(\alpha_1 - \alpha_2)](\frac{3}{8}P_0^2\cos 2\alpha) + 2\Delta(\frac{1}{\tau})\sin 2\theta_\tau(\frac{3}{8}P_0^2\cos 2\alpha)$$



where

$$\begin{split} A & \sin(4\alpha + \varphi_1) = \frac{3P_0^2}{2\tau} [-\sin(2\alpha - \alpha_1 - \alpha_2)\cos 2\alpha] \\ & + \frac{3}{8}P_0^2\Delta(\frac{1}{\tau})\cos 2\alpha \cdot [-\sin 2(\alpha - \theta_\tau - \alpha_1) \\ & + \sin 2(\alpha + \theta_\tau - \alpha_1) + \sin 2(\alpha - \theta_\tau - \alpha_2) \\ & - \sin 2(\alpha + \theta_\tau - \alpha_2)] \end{split}$$

$$\begin{split} B \, \sin(2\alpha + \varphi_2) &= \tfrac{3}{4} P_0^2 \, \cos 2\alpha [\tfrac{2}{\tau} \sin 2(\alpha_1 - \alpha_2) + \Delta(\tfrac{1}{\tau}) \sin 2\theta_\tau] \\ &+ (1 + \tfrac{3}{8} P_0^2) \Delta(\tfrac{1}{\tau}) \cdot [-\sin 2(\alpha - \theta_\tau - \alpha_1) \\ &+ \sin 2(\alpha + \theta_\tau - \alpha_1) \\ &- \sin 2(\alpha - \theta_\tau - \alpha_2) + \sin 2(\alpha + \theta_\tau - \alpha_2)] \\ &- (2 + \tfrac{3}{4} P_0^2) \Delta(\tfrac{1}{\tau}) \cdot [\sin(2\alpha + 2\theta_\tau - \alpha_1 - \alpha_2) \\ &+ \sin(2\alpha - 2\theta_\tau - \alpha_1 - \alpha_2)] \end{split}$$

$$C = \left(2 + \frac{3}{4}P_0^2\right) \Delta \left(\frac{1}{\tau}\right) \left[\sin(2\theta_\tau + \alpha_1 - \alpha_2) - \sin(2\theta_\tau - \alpha_1 + \alpha_2)\right]$$
(16c)

Error suppression method

According to Eqs. (15) and (16), the classical mode reversal³⁶ can easily eliminate the second harmonic error term. When the driving angle α is 0° and 90°, respectively:

$$\textit{BRE} = \frac{1}{2} [\Omega_{\textit{ZRO}}(0^\circ) + \Omega_{\textit{ZRO}}(90^\circ)] = k_\alpha [A \, \sin \varphi_1 + C] \eqno(17)$$

where $k_{\alpha} = \frac{1}{2nA_g} \frac{1}{4 \cos(\alpha_1 - \alpha_2)}$. Equation (17) can be expressed as the bias residual error (BRE) in classical mode reversal. For

this part of the error, when the driving angle α changes:

$$BRE(\alpha) = k_{\alpha}[A \sin(4\alpha + \varphi_1) + C] \tag{18}$$

It is natural to think that the mode reversal, combined with mode deflection, can be used to remove BRE. For HDRG, the damping $\operatorname{angle}\theta_{\tau}$ is found to be almost invariant with temperature in ref. This means that the ratio between the $\Delta(1/\tau)$ and $2/\tau$ is also almost invariable with temperature. Because the deformation caused by vibration is small relative to its geometric size, the electrode angle error α_1 and α_2 is also considered unchanged after the completion of machining. Then the derivative of Eq. (18) with respect to temperature can be expressed as:

$$\frac{d[BRE(\alpha)]}{dT} \approx k_{\alpha} \left[\frac{\partial A}{\partial T} \sin(4\alpha + \varphi_1) + \frac{\partial C}{\partial T} \right]$$
 (19)

where T is temperature. The simulation results of numerical analysis are shown in Figs. 2e, f. In FTR mode, the bias and drift are large, and the circumferential distribution is very complex. After mode reversal, the bias and drift are smaller, and the circumferential distribution is simpler. The drift can be suppressed by deflecting the gyro vibration direction to the mode angle where the drift is zero. Therefore, by setting Eq. (19) to zero, a definite α can be obtained so that the BRE is no longer sensitive to temperature. In this way, the bias drift of the gyroscope can be eliminated.

Implementation of the MRCMD control method

Figure 3 shows the control scheme of the MRCMD. Compared to the FTR control mode, the content in the black dotted box is extra. The set DA α and reversal control time sequence can be input into the FPGA. The displacement signal and the force signal pass through the deflection

matrix p and p^{-1} respectively to realize the deflection of the vibration mode. Compared with the FTR mode, the DA of the vibration mode is α . A pair of virtual switches (VS) is set between the driving loop and the sensing loop. VS can switch between option 1 and option 2 according to the set time sequence controller. When VS is in option 1, the signal received from SE enters the sensing loop, while the signal received from DE enters the driving loop. In this case, HDRG works in the state of $\alpha + 0^{\circ}$. When VS is in option 2, the signal received from DE enters the sensing loop, while the signal received from SE enters the driving loop. At this time, HDRG works in the state of $\alpha + 90^{\circ}$.

Figure 4 shows the working time sequence diagram with MRCMD of the HDRG. The gyroscope operates alternately in mode 1 ($\alpha = \alpha + 0^{\circ}$) and mode 2 ($\alpha = \alpha + 90^{\circ}$) for every constant period. The working time and transition time settings for each cycle can be found in previous work^{37,38}. The transition time is determined by the decay time of the resonant structure and the controller. The working time, on the one hand, needs to evaluate the bias characteristics of the gyroscope, and on the other hand, it needs to be balanced with the transition time to achieve a larger available data ratio. In this paper, the working time for each mode is set to 60 s, and the transition time is set to 20 s.

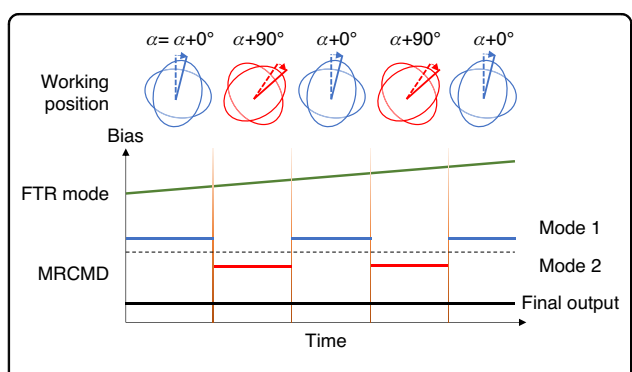


Fig. 4 Working time sequence diagram with mode reversal combined mode deflection of the HDRG. Working time sequence diagram with MRCMD of the HDRG

Calibration of DA

Based on the established error model and control system, the identification experiment of DA is performed. Firstly, the circumferential bias distribution of HDRG is tested. Since the QT electrodes are located at $\alpha = 45^{\circ}$, 135° , 225° , and 305°, the axis-tuning voltage needs to become large as DA approaches these angles. Therefore, it is necessary to turn off the quadrature control loop in Fig. 3 and use the forcecontrolled quadrature mode instead when measuring the entire circumferential bias distribution. The HDRG is fixed on a stable surface, we used a marble table. The DA α of the HDRG was changed from 0° to 720° at a rate of 2°/s. The angular rate of the output is fitted as Eq. (15). The experimental results are shown in Fig. 5a. The raw data is represented by black dots, and the fitted curve is represented by an orange curve. The second harmonic term, fourth harmonic term, and constant term represented in Eq. (15) are respectively represented by green, blue, and magenta curves. In addition, since DA changes at a rate of 2°/s, the constant term C in Eq. (15) should be the magenta curve minus $2^{\circ}/s$. It can be seen that the second harmonic term still occupies the main component of the circumferential bias. Then, the fitting residual after only second harmonic fitting and further after fourth harmonic fitting is shown in Fig. 5b. It can be seen that after the fourth harmonic fitting, the fitting residual is obviously suppressed.

Identification of DA α is performed according to Eq. (19). The condition for obtaining the target α is to make the derivative of BRE with respect to temperature zero. Select the temperature range of $[T_1, T_2]$. By integrating Eq. (19) along $[T_1, T_2]$, the drift over this temperature range can be obtained:

$$Drift(lpha) = \int_{T_1}^{T_2} rac{d[BRE(lpha)]}{dT} \ = k_{lpha}[(A_{T_2} - A_{T_1})\sin(4lpha + arphi_1) + (C_{T_2} - C_{T_1})]. \ (20)$$

Since only the fourth harmonic term and the constant term are involved in Eq. (20), there must be at least two α in

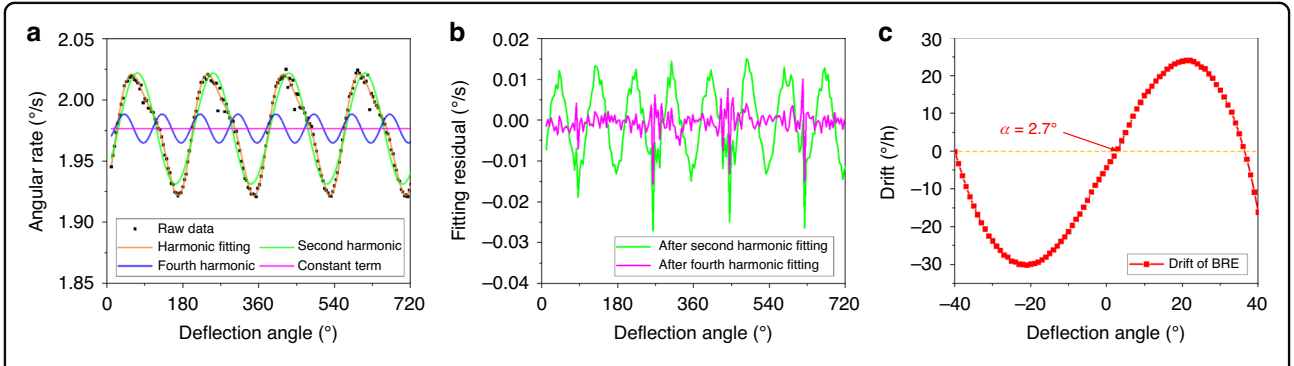


Fig. 5 Testing and fitting of circumferential bias and BRE. a Measured circumferential bias distribution of HDRG and its fitting. **b** Residual of harmonic fitting under different DAs. **c** Measured BRE drift of different DAs between T_1 and T_2

the range $[-45^\circ, 45^\circ]$ to make the drift zero. In order to avoid excessive axis-tuning voltage, the measurement range of $[-40^\circ, 40^\circ]$ is selected in this paper. Select two temperature points T_1 and T_2 , and put the gyroscope in the temperature test chamber at $\alpha = -40^\circ$, and the bias of mode 1 and mode 2 is tested, respectively. In order to reduce the impact of noise, each mode is tested for 30 s of valid data.

BRE is calculated by Eq. (17). And the average value is taken as the final result. Set the step of the DA change to 1°. The next step is to control the HDRG at $\alpha=-39^{\circ}$ and repeat the above steps until the measurement is complete in the $[-40^{\circ}, 40^{\circ}]$ range. Then set the constant temperature in the temperature test chamber to T_2 , and repeat the test. In this paper, T_1 is set to -40° C and T_2 is set to 60° C. The BRE

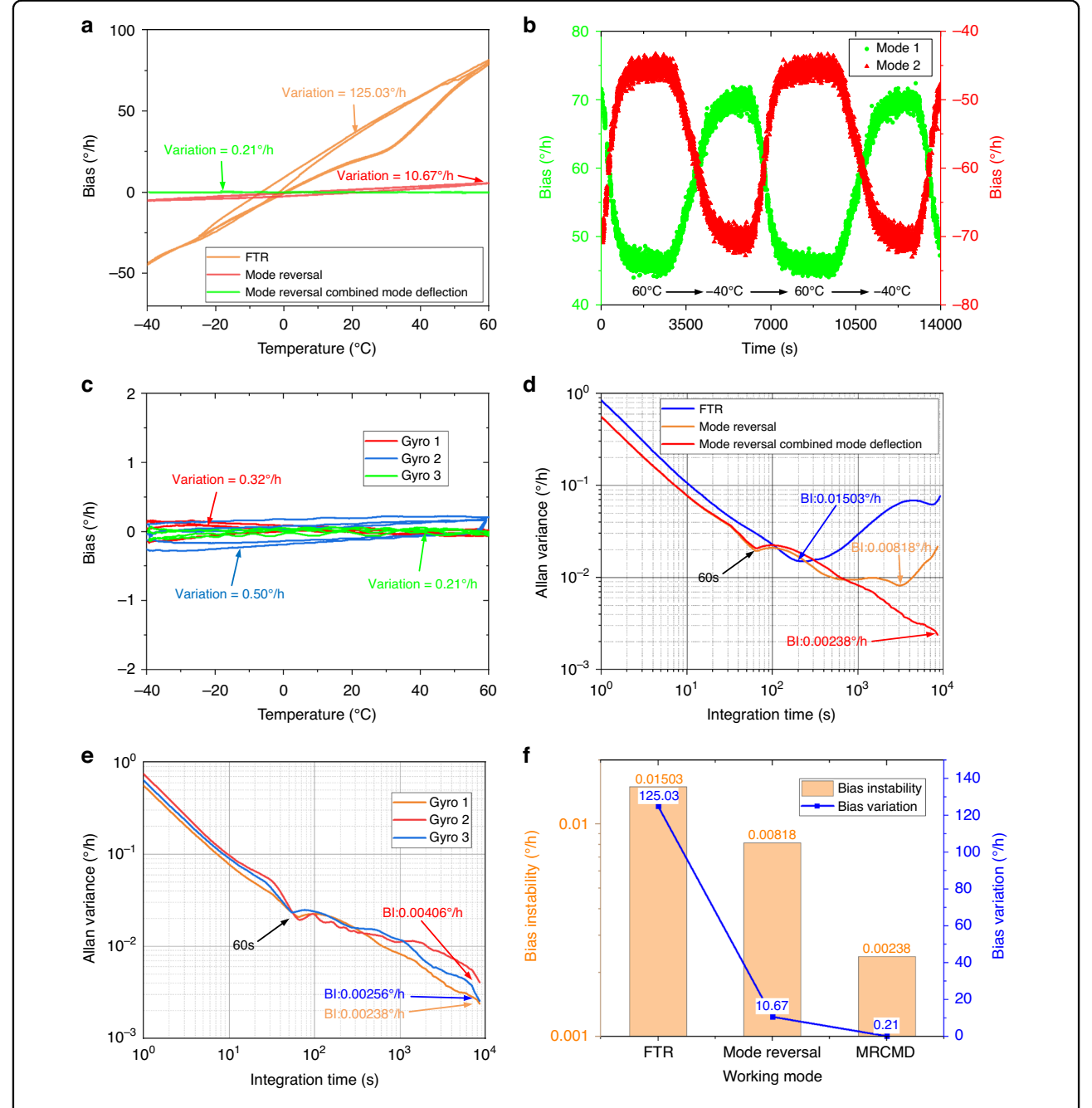


Fig. 6 The performance of the HDRG. a Tested thermal bias of the same HDRG worked in FTR mode, mode reversal, and MRCMD, respectively. b The thermal bias test data of the two modes worked in MRCMD. c Tested the thermal bias of three HDRGs that worked in MRCMD. d Tested Allan variance of the same HDRG worked in FTR mode, mode reversal, and MRCMD, respectively. e Tested the Allan variance of three HDRGs that worked in MRCMD. f Bl and bias variation of the HDRG worked in FTR mode, mode reversal, and MRCMD, respectively

Work	Туре	Operating mode	Temperature range (°C)/bias variation (°/h)	BI (°/h)
39	Disc	FTR/mode reversal	=	0.012
40	Dual mass	FTR	-	0.016
41	Tuning fork	Open-loop sense	-	0.02
4	Tuning fork	Open-loop sense	35 to 85/<0.4	< 0.02
42	Dual suspended masses	FTR/whole-angle	40 to 90/<0.7	0.007
43	Disc	FTR	-	0.04
44	Micro-shell	Whole-angle	-	0.029
17	HDRG	Mode deflection	-40 to 60/1.22	0.014
This work	HDRG	MRCMD	-40 to 60/0.34	0.003

Table 1 Performance summary of the MEMS gyroscopes

drift measured between T_1 and T_2 is shown in Fig. 5c. It can be seen that the curve has three points of intersection with 0, so the choice of DA is not fixed. Generally, the intersection closer to $\alpha=0^\circ$ has the least nonlinearity of capacitance detection when there is no angular velocity input. Therefore, $\alpha=2.7^\circ$ it is selected in this paper.

Gyroscope performance characterization

In order to verify the effectiveness of MRCMD, the thermal bias of the HDRG was tested under temperature cycling conditions ranging from -40 °C to +60 °C. The rate of temperature variation is set at 1 °C/min. Two temperature cycles were tested when the same HDRG worked in FTR mode, mode reversal, and MRCMD, respectively, and the results are shown in Fig. 6a. For ease of observation, the data were moving averaged for 100 s. In FTR mode, the bias variation is 125.03°/h, while in mode reversal, the bias variation is reduced to 10.67°/h. When operating at MRCMD, the bias variation is further reduced to 0.21°/h. The test data of the two modes are shown in Fig. 6b. It can be seen that after mode deflection, the bias variation of the two modes becomes very symmetrical, so further mode reversal can get better results. In addition, in order to verify the universality of the method, two temperature cycles are tested on all three HDRGs operating at MRCMD. For ease of observation, the data were moving averaged for 1000 s. As shown in Fig. 6c, the bias variations of the three gyroscopes are respectively 0.32°/h, 0.50°/h, and 0.21°/h. The average bias variation is 0.34°/h. The bias thermal drift is well eliminated.

The BI of the same HDRG operating in FTR, mode reversal, and MRCMD was tested at room temperature. Each bias test lasts for more than 17,000 s. As shown in Fig. 6d, in the FTR mode, the BI is 0.01503°/h, while in mode reversal, the BI is reduced to 0.00818°/h. When operating at MRCMD, the BI is further reduced to 0.00238°/h at integration times of 8500 s. In addition, it is

also verified on three HDRGs. As shown in Fig. 6e, the BI at room temperature is 0.00406°/h, 0.00256°/h, and 0.00238°/h, respectively. The average BI reaches 0.003°/h at integration times of 8500 s, which, to the best of the authors' knowledge, is the best average BI for MEMS gyroscopes reported to date. Even more excitingly, the BI still has the potential to be further reduced because the slopes of the curves remain negative when approaching 8500 s.

Under different operating modes, the room temperature BI and the bias variation under temperature cycle of HDRG are shown in Fig. 6f. It can be seen that the method proposed in this paper has a significant effect on improving the precision of the gyroscope, and this method is universal. The reported performance of MEMS gyroscopes in different operating modes is shown in Table 1. Compared with other high-precision MEMS gyroscopes, it can be found that the MRCMD method proposed in this paper improves the gyroscope performance to a new level.

Discussion

In this paper, a new control method of the MEMS gyroscope with MRCMD is proposed to improve the BI and thermal drift. In addition to the anisotropic stiffness and anisotropic damping error that are often discussed. This paper explores even smaller errors in a MEMS gyroscope that is actually fabricated. Specifically, the zerorate output model of the gyroscope is obtained when the electrode machining error and capacitance detection nonlinear error are coupled together. The MRCMD control scheme is proposed according to the bias circumferential output regularity. And the identification of DA is realized by using the circumferential bias output after mode reversal. The experimental results show that the new control method is effective in eliminating thermal drift and improving BI. Moreover, this method has no additional hardware cost and has a driving effect on the development of higher-precision MEMS gyroscopes.

Acknowledgements

This work is supported by the National Key Research and Development Program of China under grant no. 2022YFB3207301, and in part by the National Natural Science Foundation of China under grant 62304255 and grant U21A20505.

Author contributions

Liangqian Chen performed the theoretical analysis, proposed the MRCMD method, and wrote the manuscript; Dingbang Xiao and Qingsong Li designed the honeycomb disc resonator gyroscope and readout circuit; Liangqian Chen, Tongqiao Miao, and Peng Wang designed the control scheme; Xuhui Zhang and Yang Zhang tested the gyroscope performance, and Xuezhong Wu assisted in writing and correction of the manuscript.

Conflict of interest

The authors declare no competing interests.

Supplementary information The online version contains supplementary material available at https://doi.org/10.1038/s41378-025-01011-4.

Received: 26 March 2025 Revised: 13 May 2025 Accepted: 10 June 2025 Published online: 12 August 2025

References

- Wahlström, J. & Skog, I. Fifteen years of progress at zero velocity: a review. IEEE Sens. J. 21, 1139–1151 (2021).
- Asif, G. A., Ariffin, N. H., Aziz, N. A., Mukhtar, M. H. H. & Arsad, N. True north measurement: a comprehensive review of carouseling and maytagging methods for gyrocompassing. *Measurement* 226, 114121 (2024).
- Tatar, E., Mukherjee, T. & Fedder, G. K. Stress effects and compensation of bias drift in a MEMS vibratory-rate gyroscope. J. Microelectromech. Syst. 26, 569–579 (2017)
- Johnson, B. et al. Development of a navigation-grade MEMS IMU. In Proc. IEEE International Symposium on Inertial Sensors and Systems 1–4 (INERTIAL, 2021).
- Lynch, D. D. Vibratory gyro analysis by the method of averaging. In Proc. 2nd St. Petersburg Conference on Gyroscopic Technology and Navigation 26–34 (ScienceOpen, Inc., 1995).
- Cui, J., Zhao, Q. & Yan, G. Effective bias warm-up time reduction for MEMS gyroscopes based on active suppression of the coupling stiffness. *Microsyst. Nanoeng.* 5, 1–12 (2019).
- Guo, K et al. Damping asymmetry trimming based on the resistance heat dissipation for coriolis vibratory gyroscope in whole-angle mode. *Micro-machines* 11, 10 (2020).
- 8. Zhuo, M. et al. Damping tuning in the disk resonator gyroscope based on the resistance heat dissipation. In *Proc. IEEE Sensors* 1–4 (IEEE, 2019).
- Zhao, Y., Shi, Q., Xia, G. & Qiu, A. Low-noise quality factor tuning in nondegenerate MEMS gyroscope without dedicated tuning electrode. *IEEE Trans. Ind. Electron.* 71, 4230–4240 (2024).
- Cui, J. & Zhao, Q. Thermal stabilization of quality factor for dual-axis MEMS gyroscope based on joule effect in situ dynamic tuning. *IEEE Trans. Ind. Electron.* 71, 1060–1068 (2024).
- 11. Ren, J., Zhou, T., Zhou, Y., Li, Y. & Su, Y. An automatic q-factor matching method for eliminating 77% of the ZRO of a MEMS vibratory gyroscope in rate mode. *Microsyst. Nanoeng.* **10**, 67 (2024).
- Ahn, C. et al. On-chip ovenization of encapsulated disk resonator gyroscope (drg). In Proc. 2015 Transducers—2015 18th International Conference on Solid-State Sensors, Actuators and Microsystems 39–42 (TRANSDUCERS, Anchorage, 2015)
- Yang, D. et al. A micro oven-control system for inertial sensors. J. Microelectromech. Syst. 26, 507–518 (2017).
- Ge, H. H., Liu, J. Y. & Buchanan, B. Bias self-calibration techniques using silicon disc resonator gyroscope. In Proc. 2015 IEEE International Symposium on Inertial Sensors and Systems 1–4 (ISISS, Hapuna Beach, 2015); https://doi.org/10.1109/ ISISS.2015.7102375
- Trusov, A. A., Phillips, M. R., Mccammon, G. H., Rozelle, D. M. & Meyer, A. D. Continuously self-calibrating CVG system using hemispherical resonator gyroscopes. In Proc. 2015 IEEE International Symposium on Inertial Sensors and

- Systems (ISISS) 1–4 (IEEE, Hapuna Beach, 2015); https://doi.org/10.1109/ISISS. 2015.7102362
- Miao, T. et al. Virtual rotating MEMS gyrocompassing with honeycomb disk resonator gyroscope. IEEE Electron Device Lett. 43, 1331–1334 (2022).
- Wang, P. et al. Bias thermal stability improvement of mode-matching MEMS gyroscope using mode deflection. J. Microelectromechan. Syst. 32, 1–3 (2023).
- Gunhan, Y. & Unsal, D. Polynomial degree determination for temperature dependent error compensation of inertial sensors. In Proc. 2014 IEEE/ION Position, Location and Navigation Symposium—PLANS 2014 1209–1212 (IEEE, Monterey 2014).
- Shiau, J. K., Ma, D. M., Huang, C. X. & Chang, M. Y. MEMS gyroscope null drift and compensation based on neural network. *Adv. Mater. Res.* 255–260, 2077–2081 (2011).
- Araghi, G. & Landry, R. J. Temperature compensation model of MEMS inertial sensors based on neural network. In *Proceedings of the 2018 IEEE/ION Position, Location and Navigation Symposium (PLANS)* 301–309 (IEEE, Monterey, 2018).
- Chong, S. et al. Temperature drift modeling of MEMS gyroscope based on genetic-Elman neural network. *Mech. Syst. Signal Process.* 72, 897–905 (2016).
- Marolleau, E., Martin, P., Rouchon, P. & Ullah, P. Can a perfect vibratory gyroscope provide a drift-free angle estimation? In 2024 DGON Inertial Sensors and Applications (ISA) 1–20 (ISA, Braunschweig, 2024); https://doi.org/10.1109/ISA62769.2024.10786089
- Wang, P. et al. Calibration and compensation of the misalignment angle errors for the disk resonator gyroscopes. In 2020 IEEE International Symposium on Inertial Sensors and Systems (INERTIAL) 1–3 (IEEE, Hiroshima, 2020); https://doi. org/10.1109/INERTIAL48129.2020.9090094
- Ruan, Z., Ding, X., Qin, Z. & Li, H. Compensation of assembly eccentricity error of micro hemispherical resonator gyroscope. In 2021 IEEE International Symposium on Robotic and Sensors Environments (ROSE) 1–5 (IEEE, Florida, 2021); https://doi.org/10.1109/ROSE52750.2021.9611757
- Ruan, Z., Ding, X., Gao, Y., Qin, Z. & Li, H. Analysis and compensation of bias drift of force-to-rebalanced micro-hemispherical resonator gyroscope caused by assembly eccentricity error. J. Microelectromechan. Syst. 32, 16–28 (2023).
- Sun, J. et al. Investigation of angle drift induced by actuation electrode errors for whole-angle micro-shell resonator gyroscope. *IEEE Sens. J.* 22, 3105–3112 (2022)
- Wang, P. et al. Scale factor self-calibration of MEMS gyroscopes based on the high-order harmonic extraction in nonlinear detection. *IEEE Sens. J.* 22, 21761–21768 (2022).
- Li, Q. et al. Nonlinearity reduction in disk resonator gyroscopes based on the vibration amplification effect. IEEE Trans. Ind. Electron. 67, 6946–6954 (2020).
- Li, Q. et al. A novel nonlinearity reduction method in disk resonator gyroscopes based on the vibration amplification effect. In 2019 20th International Conference on Solid-State Sensors, Actuators and Microsystems & Eurosensors XXXIII 586–589 (TRANSDUCERS & EUROSENSORS, Berlin, 2019); https://doi.org/ 10.1109/TRANSDUCERS.2019.8808704
- Sun, J. et al. 0.79 ppm scale-factor nonlinearity whole-angle microshell gyroscope realized by real-time calibration of capacitive displacement detection. *Microsyst. Nanoeng.* 7, 79 (2021).
- Xu, Y. et al. Stiffness-mass decoupled honeycomb-like disk resonator gyroscope. In 2019 IEEE 32nd International Conference on Micro Electro Mechanical Systems (MEMS) 656–659 (MEMS, Seoul, 2019); https://doi.org/10.1109/ MEMSYS.2019.8870838
- Xu, Y. et al. Honeycomb-like disk resonator gyroscope. IEEE Sens. J. 20, 85–94 (2020).
- Xu, Y. et al. 0.015 degree-per-hour honeycomb disk resonator gyroscope. *IEEE Sens. J.* 21, 7326–7338 (2021).
- Chen, L. et al. A temperature drift suppression method of mode-matched MEMS gyroscope based on a combination of mode reversal and multiple regression. *Micromachines* 13, 10 (2022).
- 35. Liu, J. Y. & Challoner, A. D. Electronic bias compensation for a gyroscope (Continuation—InPart). US Patent Application, Jan 31 (2013).
- Ge, H. H., Liu, J. Y. & Buchanan, B. Bias self-calibration techniques using silicon disc resonator gyroscope. In 2015 IEEE International Symposium on Inertial Sensors and Systems 1–4 (INERTIAL, Hapuna Beach, 2015); https://doi.org/10. 1109/ISISS.2015.7102375
- Chen, L. et al. A time-series configuration method of mode reversal in MEMS gyroscopes under different temperature-varying conditions. In 2023 IEEE 36th International Conference on Micro Electro Mechanical

- Systems (MEMS) 849–852 (IEEE, Munich, 2023); https://doi.org/10.1109/MEMS49605.2023.10052326
- 38. Miao, T. et al. Removal of the rate table: MEMS gyrocompass with virtual maytagging. *Microsyst. Nanoeng.* **9**, 138 (2023).
- Challoner, A. D., Ge, H. H. & Liu, J. Y. Boeing disc resonator gyroscope. In Proc. IEEE/ION Position, Location Navigat. Symp. (PLANS) 504–514 (IEEE, Monterey, 2014); https://doi.org/10.1109/PLANS.2014.6851410
- Koenig, S. et al. Towards a navigation grade Si-MEMS gyroscope. In 2019 DGON Inertial Sensors and Systems (ISS) 1–18 (ISS, Braunschweig, 2019); https://doi.org/10.1109/ISS46986.2019.8943770
- Gadola, M. et al. 1.3 mm² nav-grade NEMS-based gyroscope. J. Microelectromechan. Syst. 30, 513–520 (2021).
- 42. Emerard, J. D. et al. Si-MEMS gyro by Safran: towards the navigation grade. In 2022 IEEE International Symposium on Inertial Sensors and Systems (INERTIAL) 1–4 (IEEE, Avignon, 2022); https://doi.org/10.1109/INERTIAL53425. 2022.9787731
- 43. Li, Q. et al. 0.04 degree-per-hour MEMS disk resonator gyroscope with high-quality factor (510 k) and long decaying time constant (74.9 s). *Microsyst. Nanoeng.* **4**, 32 (2018).
- 44. Yu, S. et al. Real-time correction of gain nonlinearity in electrostatic actuation for whole-angle micro-shell resonator gyroscope. *Microsyst. Nanoeng.* **10**, 164 (2024)